Concatenated Vertical Channel Modeling and Performance Analysis for HAP-based Optical Networks

Neha Tiwari, Swades De, and Dharmaraja Selvamuthu

***Abstract*—In this paper, we look into the modeling of free space optical channel and design of the HAP-based wireless optical networks. For vertical beam propagation, the pressure and temperature gradients alter with height. Microscale variations in refractivity result in uncertainties that depend on elevation. As a result, irradiance fading variance caused by turbulence keeps on changing throughout the propagation path. Also, the eddies' shape transitions from spherical and symmetrical near the ground to highly asymmetrical and anisotropic at heights far away from the ground. In this paper, taking into account these variations concerning height, we propose to break the vertical FSO (VFSO) channel into parallel layers. We develop a VFSO channel model built upon the cascaded structure of fading coefficients. Correlated phase screen simulation method is used to verify the accuracy of the proposed channel model. Next, a closed-form expression for the probability density function is developed for the concatenated channel incorporating a generalized pointing error model. To demonstrate the significance of this newly developed VFSO channel model in HAP-based optical networks, closed-form expressions for bit error rate performance is also derived. Monte Carlo simulations substantiate that the newly formulated analytical expressions offer accurate assessments of the BER performance for HAP-based VFSO links. For HAP-based optical networks facing weak turbulence, the newly developed expressions provide an accuracy of about 2 dB for a BER of 10^{-4} as compared to the existing competitive models. This value increases to 4 dB after incorporating pointing errors in HAP-based optical networks. In optical networks facing strong fluctuation regions, the newly developed expressions provide an accuracy of about 8 dB for a BER of 10^{-4} as compared to the existing competitive model. Similar observations are made after incorporating pointing errors in HAP-based optical networks facing strong turbulence regions.**

***Index Terms*—Anisotropic eddies, bit error rate performance, high altitude platforms (HAPs), pointing error, turbulence channel model, vertical free space optical (FSO) links.**

I. Introduction

In order to provide the users with broadband connectivity at a low cost, high-altitude platforms (HAPs) present a promising communication alternative as it combines the benefits of terrestrial and satellite communication systems. HAPs are airships or airplanes that are typically positioned at 17 to 25 km height in the stratosphere [2], [3]. To aid HAP connectivity with the ground nodes, e.g., terrestrial base stations, free-space optics is a viable alternative to radio-frequency (RF) technology [4] as it offers a significantly higher operational bandwidth. Hence, for the future wireless networks, integrating HAPs using free space optical (FSO) communications can help in achieving high data rate connectivity. Various HAP networks, namely, Helios in the U.S., Skynet in Asia, STRATOS, HALE, HeliNet, HAPCOS, CAPANINA in Europe, have been deployed successfully [5], [6]. Two recent projects that use FSO communication for HAP connectivity are Facebook's Internet delivery drone and Google's Project Loon [7], [8]. FSO links suffer from two main difficulties that are required to be sorted for reliable and efficient communication.

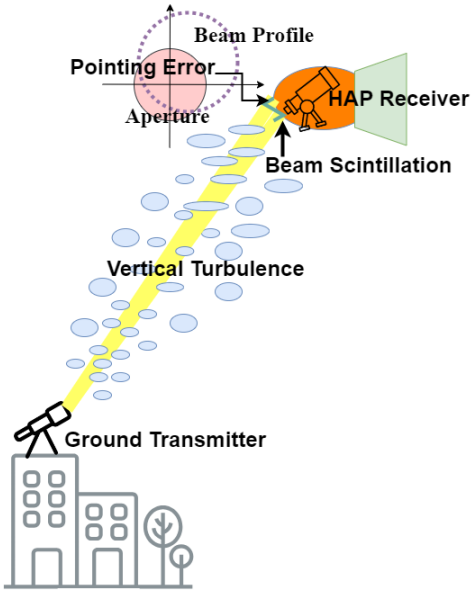

Figure 1: Ground-HAP FSO system model affected by vertical turbulence.

First, the implementation of HAP-based FSO links is difficult due to space constraints. Variations in temperature and pressure within Earth's atmosphere give rise to microscale fluctuations in refractivity resulting in uncertainties that depend on elevation. This result in vertical turbulence characterized by formation of eddies as depicted in Fig.1. Refractivity fluctuations are most pronounced near the ground

N. Tiwari is with Bharti School of Telecommunication and Management, IIT Delhi, New Delhi, India (email: bsz208010@dbst.iitd.ac.in). S. De is with Department of Electrical Engineering and Bharti School of Telecommunication and Management, IIT Delhi, New Delhi, India (email: swadesd@ee.iitd.ac.in). D. Selvamuthu is with Department of Mathematics and Bharti School of Telecommunication and Management, IIT Delhi, New Delhi, India (email: dharmar@maths.iitd.ac.in).

A preliminary version of the work has been accepted in 29th National Conference on Communications, 2023 [1].

and decreases as the altitude increases. Also, at higher altitudes from the earth's surface, eddy size in the atmosphere increases. At higher altitudes, the shape of the eddies also undergoes a transformation, from a spherical and symmetrical form near the ground to an increasingly asymmetrical and anisotropic configuration at heights far above the ground [9].
Second, the performance of FSO links is hindered by pointing errors arising from a mismatch between the transmitter and receiver [10], [11]. This limitation is particularly challenging for HAP based FSO links in comparison to communication between two fixed points as in terrestrial networks. Atmospheric turbulence causes fluctuations in the optical beam wavefront (beam scintillation) and pointing errors in the received signal, which directly affect the bit error rate (BER). Hence, to fully exploit the advantages of a ground-to-HAP vertical FSO (VFSO) link, it is necessary to accurately characterize this communication channel. This involves precise modeling of the received signal strength in the presence of atmospheric turbulence and pointing errors which is the main focus of this paper.

A. Literature Survey

Channel models in FSO communications play a crucial role in predicting and understanding the optical communication links performance. Several models exist describing the fading arising from atmospheric turbulence in both weak and strong scenarios. These include the lognormal, gamma-gamma, Exponentiated Weibull (EW), lognormal-Rician, Málaga and K distributions [12], [13]. However, there are certain lacunae or limitations in these models which are highlighted below:

1) *Simplified Assumptions*: The existing FSO channel models rely on simplified assumptions on the atmosphere and environmental conditions. For instance, they consider a homogenous atmosphere i.e., the statistical properties of turbulence do not change throughout the entire channel [14]–[16]. This does not accurately represent the practical VFSO communication scenarios where atmospheric turbulence can vary significantly with altitude and weather conditions.
2) *Narrow Applicability:* Most of these models have limited applicability to specific scenarios. For example, the lognormal model is suitable for weak turbulence conditions but may not accurately represent strong turbulence conditions commonly encountered in certain regions or at lower altitudes. In moderate-to-strong fading conditions, Gamma-gamma distribution suits well [17], [18] but it's accuracy is surpassed by lognormal-Rician distribution which has shown excellent agreement with experimental data across all turbulence conditions (weak, moderate and strong) [13], [19].
3) *Complexity versus Accuracy Trade-off:* Advanced FSO models, like the lognormal-Rician model, are quite complex to implement and require numerous parameters and for them balancing model complexity with accuracy is challenging. Another limitation associated with the lognormal-Rician model is the lack of understanding regarding the relationship between its empirical parameters with the turbulent atmosphere. This poses a challenge in accurately determining the model parameters based on the atmospheric conditions. Also, its probability distribution function (PDF) expression has an integral form which makes it intractable for developing closed-form expressions. A recently proposed turbulence model called Málaga has gained attention for its ability to generalize several turbulence models [20], [21]. However, it falls short in fitting weak turbulence scenarios when compared to lognormal-Rician channels. This is due to Málaga utilizing Gamma distribution as an approximation for the lognormal distribution, which may affect the modeling accuracy [22].
4) *Absence of Non-Kolmogorov Turbulence:* An important drawback in the usefulness of current channel models [17], [19], [20] for VFSO environments lies in their heavy reliance on the Kolmogorov turbulence model to depict atmospheric turbulence effects. In reality, atmospheric turbulence demonstrates deviation from the Kolmogorov model, especially in scenarios with non-uniform and anisotropic conditions. Therefore, there is a pressing need to integrate the characteristics of non-Kolmogorov turbulence into VFSO channel models to improve their accuracy.
5) *Underwater turbulence studies*. Authors in [23], [24] have incorporated the gradient of temperature and salinity changes while characterizing the underwater turbulence. However, the medium responsible for inducing stochastic fluctuations in the refractive index of underwater differs from that in the atmosphere. Water is denser and more viscous compared to air, because of which underwater turbulence tends to have slower fluctuations and longer-lasting effects compared to atmospheric turbulence. Air on the other hand is less dense and less viscous, resulting in faster fluctuations and shorter-lasting effects and there is no study present in the literature that deals with characterizing varying strength of atmospheric turbulence.

In summary, while various FSO channel models exist in the literature for capturing atmospheric turbulence-induced fading, each has its own limitations. Further research and refinement are needed to improve their accuracy and applicability.

In addition to turbulence-induced fading, recently there has been some studies on pointing error induced losses. In [25], a comprehensive channel model is presented for a small aerial FSO link, focusing on the impact of platform vibrations. Building upon the system described in [25], the authors in [26] refined their findings further by deriving a manageable channel model. To characterize the pointing error the most popular models in literature include the Rayleigh, Rician, Hoyt, and Beckmann distributions [27], [28], [29]. For instance, the authors in [30], [31] considered strong turbulence and used Rayleigh distribution to model the pointing error. The authors in [22], [32], [33] have also considered Rayleigh distribution to model pointing error. It is worth noting that Beckmann serves as a general framework, encompassing the other three distributions as special cases and will be used in this work. Summary of research conducted on the joint impacts

Table I: Summary of studies on the joint effect of atmospheric turbulence and pointing error

Turbulence model	Pointing error model	Performance metrics	Related paper
lognormal (LN), gamma gamma (GG)	Rician	Capacity, outage probability (OP), BER	[14], [15], [34]
doubly inverted GG	Rician	Capacity, OP, BER	[18]
Málaga	Rayleigh	OP, BER	[21], [29]
Málaga	Rayleigh	OP, BER, Capacity	[22]
lognormal-rician	Beckmann	Capacity, OP, BER	[19]
GG	Hoyt	BER	[28]
GG	Rayleigh	OP, BER	[35]
GG	approximate Beckmann	OP, BER	[36]
LN,GG	Beckmann	Capacity	[37]
LN, GG, EW, double gamma	Rayleigh	OP, Capacity, BER	[30], [32], [33], [38]
GG	Beckmann	OP, BER	[39]
Concatenated LN, GG	approximate Beckmann	BER	This Work

of atmospheric turbulence along with pointing errors is given in Table I.

B. Motivation

In this paper we formulate a concatenated vertical channel model for HAP-based optical networks keeping in mind that the vertical turbulence strength in the atmosphere keeps varying as vertical distance increases. The atmosphere exhibits variations in temperature and pressure with height, as depicted in Fig. 2.

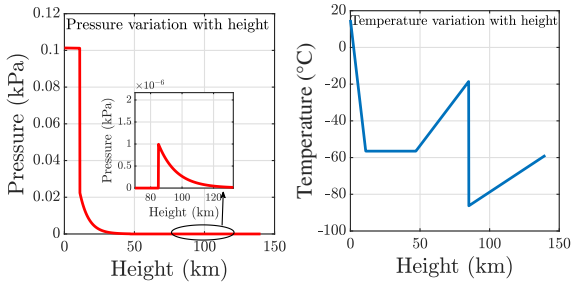

Figure 2: Pressure and temperature variation with height based on the U.S. Standard Atmosphere, 1976 [40].

These variations in atmospheric conditions result in microscale fluctuations in refractivity, introducing uncertainties that depend on the elevation. The changes in refractive index subsequently impact the turbulence-induced fading. Furthermore, as the distance increases from the ground, the characteristics of eddies shift from being spherical and symmetrical to becoming significantly asymmetrical and anisotropic [9]. This shift highlights the heterogeneous nature of turbulence at varying altitudes. Therefore, for VFSO link, the turbulence strength changes throughout the transmission range and this essential factor has been accounted in our proposed VFSO channel model. The concatenated vertical channel model is developed based on following definition:

Definition 1. *Atmospheric stratification refers to the vertical layering of the earth's atmosphere based on variations in temperature, pressure and other properties with height.*

In the proposed channel model we take into account this stratification which is crucial for modeling and predicting the characteristics of turbulence. In vertical environments the presence of strong atmospheric stratification are characterized into distinct non-mixing layers which are arranged on the basis of their densities such that the less dense layers are positioned above the denser ones. As a result, the fading induced by turbulence in these layers can be statistically treated as independent phenomena, each characterized by its own set of parameters. This enables a more accurate modeling and analysis of the impact of turbulence on VFSO communication systems.

C. Contributions

In our preliminary study [1], we investigated the impact of changing refractive fluctuations and eddies present in optical communication channel between ground and HAPs. One significant outcome of our analysis was about the impact that the typical maximum size and shape of individual eddies adjacent to the optical receiver have on the received optical beam power profile. Although we characterized beam irradiance at different heights using phase screen simulations, we did not derive analytical expressions for the PDFs. As a comprehensive study, in this paper we focus on deriving analytical channel models by considering the impact of varying turbulence, specifically the lognormal and gamma-gamma turbulence models, as well as the geometric loss caused by pointing errors. By incorporating these factors, our aim is to provide a comprehensive understanding of the channel characteristics in HAP based VFSO links. The primary contributions of this work include:

1) We analyze the VFSO links, taking into account the varying nature of the turbulent medium. To address this turbulence inhomogeneity, we propose a layered turbulence model for the VFSO links, where distribution of every layer is same but the parameter values of each distribution differs. We consider lognormal to model weak irradiance fading and gamma-gamma distributions for strong irradiance fading regimes.
2) Next, we develop closed-form PDF expression for concatenated lognormal and gamma-gamma channel model with generalized pointing errors model.
3) Further, we analyze BER performance of the VFSO link. We derive analytical BER expressions by incorporating the newly developed concatenated channel PDFs that account for pointing errors.
4) Finally, we demonstrate with the help of correlated phase screen simulation method that the proposed channel

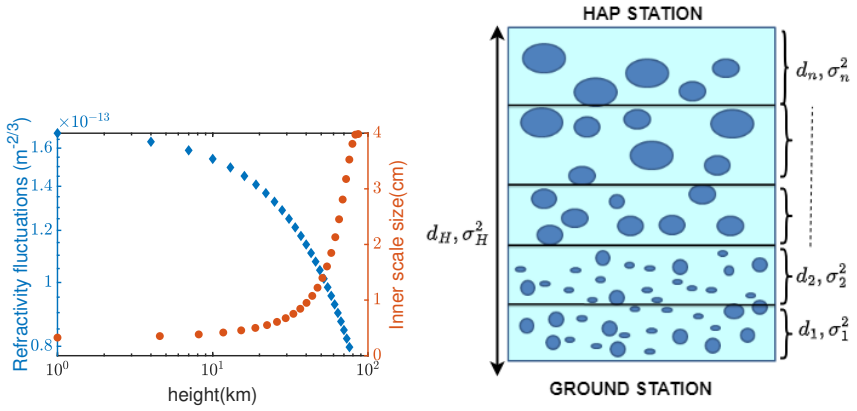

(a) (b)

Figure 3: Illustration of (a) Refractive index and eddy size variation versus height; (b) HAP-based VFSO network.

model aligns closely with the practical channel, which outperforms the existing lognormal and gamma-gamma atmospheric turbulence models.

To the best of our knowledge this is first study highlighting the accuracy and merits of layered turbulence model for VFSO link.

The subsequent sections of the paper are structured as follow: Concatenated channel model is introduced in Section II. The impact of pointing errors is discussed in Section III. BER performance analysis for the VFSO system is given in Section IV. Numerical results are presented in Section V. The paper is concluded in Section VI.

II. VFSO System and Turbulence Channel Model

The VFSO network consists of a HAP station positioned at a distance denoted as d_H from the ground station. The optical channel between the HAP and the ground is influenced by atmospheric turbulence arising from refractive index fluctuations and formation of eddies. Turbulence variance in a VFSO link changes with height because the gradient of both eddy size and refractive index variations are height dependent as depicted in Fig. 3(a). To account for these height-dependent variations, we propose to model the VFSO link as cascaded layers shown in Fig. 3(b). Each layer in this model is characterized by a unique turbulence mean and variance labeled as μ_n and σ_n^2. The thickness of each layer is optimally decided to ensure that variance change in the layer is below a given threshold ϵ . Thus, the total transmission range d_H is the sum of all d_n, where d_n denotes thickness of the n^{th} layer and $n = 1, 2, \ldots, N$. Let the multiplicative fading coefficient of the n^{th} layer be I_n . Then the overall fading coefficient is $I_H = \prod_{n=1}^{N} I_n$ [41]. Here, fading coefficients of one layer is considered independent of other layer, which is justifiable due to atmospheric stratification.

The gradual and complex variations of atmospheric conditions in proposed VFSO channel is captured using altitude-dependent parameters like refractive index fluctuations C_n^2, outer scales size L_0, inner scales size l_0, to reflect the varying nature of atmospheric turbulence. To obtain the refractive index structure of the atmosphere we have used the famous Hufnagel-Valley $(H - V_{5/7})$ model [42]. To model L_0 and l_0 as a function of altitude h, the empirical Coulman-Vernin profile is used [43], [44].

A. Modeling weak turbulence channel as $N\star$ generalized lognormal distribution

For a ground-based transmitter, HAP receivers are located in a region of weak turbulence characterized by $C_n^2 < 10^{-17} m^{-2/3}$. In such conditions the irradiance PDF follows a lognormal distribution due to weak irradiance fluctuations. Thus, in this scenario, the n^{th} layer fading coefficient I_n follows a lognormal distribution. Let μ_{x_n} be the mean and $\sigma_{x_n}^2$ represent the log-irradiance variance of n^{th} layer. $X_n = 0.5 \ln I_n$ is log-amplitude coefficient of n^{th} layer. Its PDF can be expressed as [13]

$$p_{I_n}(I_n) = \frac{1}{I_n \sqrt{2\pi(4\sigma_{x_n}^2)}} \exp\left[-\frac{[\ln(I_n) - 2\mu_{x_n}]^2}{2(4\sigma_{x_n}^2)}\right], I_n > 0 \tag{1}$$

where $\sigma_{x_n}^2$ can be expressed in terms of scintillation index $\sigma_{I_n}^2$ as

$$\sigma_{x_n}^2 = 0.25 \ln(\sigma_{I_n}^2 + 1). \tag{2}$$

The fading envelope is normalized and $\mathbb{E}[I_n] = 1$, which gives $\mu_{x_n} = -\sigma_{x_n}^2$ [45]. With this it is ensured that the fading coefficients do not change average power value.

Preposition 1. *The PDF of the overall fading coefficient $I_H = \prod_{n=1}^{N} I_n$ follows lognormal distribution, given by*

$$p_{I_H}(I_H) = \frac{1}{I_H \sqrt{2\pi(\sigma_H^2)}} \exp\left[-\frac{[\ln(I_H) - \mu_H]^2}{2\sigma_H^2}\right], I_H > 0. \tag{3}$$

In (3), $\mu_H = \sum_{n=1}^{N} 2\mu_{x_n}$ and $\sigma_H^2 = \sum_{n=1}^{N} 4\sigma_{x_n}^2$. It is important to note that an assumption is made that the fading

coefficients I_i and I_j, where i and j can take values from 1 to N, are independent but not necessarily identically distributed. This assumption allows us to compute the overall variance, which is obtained by summing up the variances of the fading coefficients of all individual layers.

Proof. Consider two independent random variables: X following a lognormal distribution having μ_x and σ_x as mean and standard deviation respectively, Y following a lognormal distribution having μ_y and σ_y as mean and standard deviation respectively. Let $V = XY$. According to the properties of lognormal distributions, the distribution of V is also lognormal with mean $\mu_x + \mu_y$ and variance $\sigma_x^2 + \sigma_y^2$.

This property can be extended to find the PDF of product of N generalized lognormally distributed random variables, given by (3), where the parameters are obtained as the sum of the parameters of the individual distributions. □

Complexity Analysis: The complexity of evaluating the PDF for a single lognormal distribution involves evaluating the natural logarithm, squaring and multiplying terms and computing the exponential function. Given that these are standard mathematical functions, the complexity is $\mathcal{O}(1)$ for each value of I_n. To evaluate the PDF of the cascaded lognormal distribution we begin with computing the parameters μ_H and σ_H^2, which involves summing over N layers. This has a complexity of $\mathcal{O}(N)$. Then we evaluate the lognormal PDF for I_H, which involves logarithmic and exponential operations, with a complexity of $\mathcal{O}(1)$ for each value of I_H. Thus, the overall complexity for evaluating the PDF of the cascaded lognormal distribution is $\mathcal{O}(N)$.

B. Modeling strong turbulence channel as $N\star$ generalized gamma-gamma distribution

For HAP transmitter, the ground receivers are embedded in strong turbulence region ($C_n^2 > 10^{-13} m^{-2/3}$). Under these conditions, the fading coefficient I_n for the n^{th} layer is modelled as gamma-gamma distribution [13].

$$p_{I_n}(I_n) = \upsilon I_n^{\frac{(\alpha_n+\beta_n)}{2}-1} K_{\alpha_n-\beta_n}(2\sqrt{\alpha_n\beta_n I_n}); I_n > 0 \quad (4)$$

where $\upsilon = \frac{2(\alpha_n\beta_n)^{(\alpha_n+\beta_n)/2}}{\Gamma(\alpha_n)\Gamma(\beta_n)}$, α_n and β_n are large-scale and small-scale scintillation parameters, respectively, for the n^{th} and $K_\nu(\cdot)$ is the modified Bessel function of the second kind and order ν. For plane wave propagation,

$$\alpha_n = \left[\exp\left(\frac{0.49\sigma_{I_n}^2}{(1+1.11\sigma_{I_n}^{12/5})^{7/6}}\right) - 1\right]^{-1} \quad (5)$$

$$\beta_n = \left[\exp\left(\frac{0.51\sigma_{I_n}^2}{(1+0.69\sigma_{I_n}^{12/5})^{5/6}}\right) - 1\right]^{-1}. \quad (6)$$

The log-irradiance variance $\sigma_{x_n}^2$ can be expressed in terms of scintillation index $\sigma_{I_n}^2$ as

$$\sigma_{x_n}^2 = \exp\left[\frac{0.49\sigma_{I_n}^2}{(1+1.11\sigma_{I_n}^{12/5})^{7/6}} + \frac{0.51\sigma_{I_n}^2}{(1+0.69\sigma_{I_n}^{12/5})^{5/6}}\right] - 1. \quad (7)$$

Theorem 1. *For a product of N independent and non identically distributed gamma-gamma random variables the PDF is obtained as*

$$p_{I_H}(I_H) = \Upsilon G_{0,2N}^{2N,0}\left(\left(\prod_{n=1}^{N}(\alpha_n\beta_n)\right) I_H \middle| \begin{matrix}\cdots \\ \Xi\end{matrix}\right). \quad (8)$$

where $\Upsilon = \frac{\prod_{n=1}^{N}(\alpha_n\beta_n)}{\prod_{n=1}^{N}(\Gamma(\alpha_n)\Gamma(\beta_n))}$ *and* $\Xi = \alpha_1 - 1, \ldots, \alpha_N - 1, \beta_1 - 1, \ldots, \beta_N - 1$

Proof. See Appendix A. □

Complexity Analysis: The complexity of evaluating the PDF of a single gamma-gamma distribution involves evaluating the power $I_n^{\frac{(\alpha_n+\beta_n)}{2}-1}$ and the modified Bessel function $K_{\alpha_n-\beta_n}(2\sqrt{\alpha_n\beta_n I_n})$. Both these operations have a complexity of $\mathcal{O}(1)$ for each evaluation. To evaluate the PDF of the cascaded gamma-gamma distribution, first we have to compute the parameters α_n and β_n for each layer n, resulting in $\mathcal{O}(N)$ complexity. Computation of the product and ratios for Υ, involves $\mathcal{O}(N)$ operations. Evaluating the Meijer G-function $G_{0,2N}^{2N,0}$, is computationally intensive. The best case complexity is $\mathcal{O}(N)$. Thus, the overall complexity for the cascaded gamma-gamma distribution is $\mathcal{O}(N)$ in the best-case scenario.

C. Three-dimensional model of optical atmospheric turbulence

Since the turbulent eddies dimension span from a few millimetres to hundreds of meters, split-step propagation method [46] is used which handles both vertical and lateral variations of the refractive index fluctuations present in the atmosphere and offers a full-forward wave calculation with some approximations. However, there are a few methodological issues with the construction of artificial turbulence on the basis of phase screen model in statistical optics. With more phase screens being used in calculations, the split-step solution precision increases. However for very narrow, closely spaced screens, the Markov approximation assumptions that support the random phase screen statistics become unacceptable [47].

In this work an alternative method for creating multiple phase screens is used. It is devoid of the Markov approximation assumptions and uses stochastic representation of the 3D volume of turbulence. Sparse spectrum technique is used for generating refractive-index fluctuations with prescribed spectral density. In this work, we generate three dimensional phase screens correlated by temperature.

Remark 1. *Both two- and three-dimensional phase screens can be used in our performance study objectives. We concentrate on three-dimensional screens without losing generality and observe that the results can be easily converted to two-dimensional screens without requiring modifications to the approaches.*

The correlated phase screens (CPS) model based simulation of atmospheric turbulence is new in the literature and has excluded the need for the phase screens to be statistically independent. Recent optical communications research has used

the autocorrelation and cross correlation functions of the phase change to simulate CPS. In contrast, we produce the CPS using an analytical expression of the phase power spectral density. We have simulated the CPS using non-Kolmogorov power spectral density for turbulence.
Next section presents closed-form PDF expression development for concatenated channel model incorporating generalized pointing errors model. To validate the analytical expressions we will compare the results with the data points obtained by correlated phase screen simulations.

III. Composite Turbulence Channel Model with Pointing Errors

In this section we derive concatenated channel model by considering the combined impact of atmospheric turbulence and pointing error loss due to misalignment by taking into consideration aperture size of the detector, beam width, variance due to different jitters, the effect of nonzero boresight error and the correlation between the elevation and horizontal displacement.

A. Beam Wander Plus Transceiver Induced Extra Pointing Error:

For the untracked or slow tracked FSO communication system, the optical beam moves randomly due to the turbulence induced beam wander and the possible transceiver induced extra pointing error. The distribution of (x, y) is consisted of two random variable. One is the two dimensional beam wander (x_b, y_b) and the other is the extra random pointing error (x_p, y_p).

$$x = x_b + x_p \tag{9}$$

$$y = y_b + y_p \tag{10}$$

Beam Wander: Previous studies show that the atmospheric turbulence induced beam wander (x_b, y_b) is a two dimensional Gaussian random variable with zero mean and standard deviation ρ_b where,

$$x_b \sim \mathcal{N}(0, \rho_b^2) \tag{11}$$

$$y_b \sim \mathcal{N}(0, \rho_b^2) \tag{12}$$

and

$$\rho_b^2 = kC_n^2 D_0^{-1/3} L^3 \tag{13}$$

where C_n^2 is the refractive index structure parameter, D_0 is the transmitter aperture diameter, L is the propagation distance, k is the constant and depends on the beam profile.
Two Dimensional Gaussian Random Model: The two dimensional Gaussian random model is wildly adopted in the ground-HAP optical communication. In this model, the extra pointing error follows independent two dimensional Gaussian distribution in both x and y directions with misalignment $(\Delta x, \Delta y)$ and variance ρ_p, where

$$x_p \sim \mathcal{N}(\Delta x, \rho_p^2) \tag{14}$$

$$y_p \sim \mathcal{N}(\Delta y, \rho_p^2) \tag{15}$$

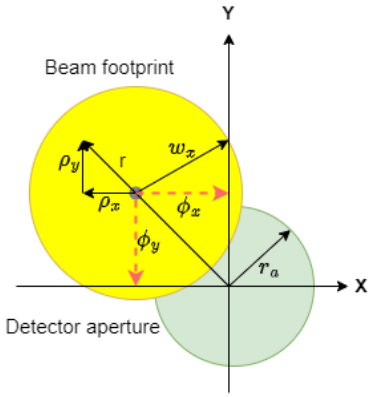

Figure 4: The received optical beam footprint. Pointing errors cause deviation from the receiver lens center.

B. Pointing error model

For a circular receiver aperture with radius r_a and a collecting area $A = \pi r_a^2$, the attenuation due to pointing error loss and geometrical spread at a propagation distance ζ is given as [30]

$$p_{I_p}(r;\zeta) \approx A_0 \exp\left(-\frac{2r^2}{w_{zeq}^2}\right), r \geq 0. \tag{16}$$

For an optical beam propagating in a turbulent medium, $w_{\zeta_{eq}} = \sqrt{\frac{w_\zeta^2 \sqrt{\pi}\text{erf}(\nu)}{2\nu \exp(-\nu^2)}}$, $\nu = \frac{\sqrt{\pi} r_a}{\sqrt{2} w_\zeta}$, $A_0 = [\text{erf}(\nu)]^2$, $w_\zeta \approx \theta_\zeta$ where θ is the transmit divergence angle. At the receiver plane, the radial displacement $||r|| = \sqrt{x^2 + y^2}$, where x and y represent the elevation and horizontal displacements of the optical beam, respectively. These displacements are considered Gaussian random variables, with x following $N(\phi_x, \rho_x)$ and y following $N(\phi_y, \rho_y)$. Importantly, in FSO applications, x and y may exhibit correlations. In that case, their joint random vector is a bivariate normal distribution, and its specific expression can be found in [19]. The probability distribution of I_p is obtained as

$$p_{I_p}(I_p) = \frac{z^2}{A_r^{z^2}} I_p^{z^2-1}, 0 \leq I_p \leq A_r. \tag{17}$$

As shown in [36], the corresponding expressions for the z and A_r are obtained by transforming correlated random variables x, y into independent random variables x', y' with corresponding mean and variance $(\phi_x^{'}, \rho_x^{'})$ and $(\phi_y^{'}, \rho_y^{'})$ and is given by

$$z^2 = \frac{w_{\zeta_{eq}}^2}{4} \left(\frac{3\phi_x^{'2}\rho_x^{'4} + 3\phi_y^{'2}\rho_y^{'4} + \phi_x^{'6} + \rho_y^{'6}}{2}\right)^{-1/3}. \tag{18}$$

$$A_r = A_0 \exp\left(\frac{1}{z^2} - \frac{1}{2\psi_x^{'2}} - \frac{1}{2\psi_y^{'2}} - \frac{\phi_x^{'2}}{2\rho_x^{'2}\psi_x^{'2}} - \frac{\phi_y^{'2}}{2\rho_y^{'2}\psi_y^{'2}}\right) \tag{19}$$

where $\psi_x^{'} = \frac{w_{\zeta_{eq}}}{2\rho_x^{'}}$, $\psi_y^{'} = \frac{w_{\zeta_{eq}}}{2\rho_y^{'}}$.

C. Statistics of the cascaded lognormal channel model with pointing error

Utilizing the Gamma approximation of the lognormal distribution [48], (3) can be written as

$$p_{I_H}(I_H) \approx \frac{1}{\Gamma(m_{I_H})}\left(\frac{m_{I_H}}{\Omega_{I_H}}\right)^{m_{I_H}} I_H^{m_{I_H}-1}\exp\left(-\frac{m_{I_H} I_H}{\Omega_{I_H}}\right). \tag{20}$$

In (20), the parameters m_{I_H} and Ω_{I_H} hold the following relations with σ_H and μ_H :

$$m_{I_H} = \frac{1}{e^{\sigma_H^2}-1} \;\; and \;\; \Omega_{I_H} = e^{\mu_H}\sqrt{\frac{m_{I_H}+1}{m_{I_H}}}$$

where m_{I_H} is the shaping parameter and Ω_{I_H} is the mean power. The joint distribution of $I = I_l I_H I_p$, where I_l is the path loss that acts as a scaling factor can be derived by utilizing

$$\begin{aligned} p_I(I) &= \int_{I/(I_l A_r)}^{\infty} p_{I_H}(I_H) p_{I|I_H}(I|I_H) dI_H \\ &= \int_{I/(I_l A_r)}^{\infty} p_{I_H}(I_H)\frac{I}{I_H I_l} p_{I_p}\left(\frac{I}{I_H I_l}\right) dI_H. \end{aligned} \tag{21}$$

In (21), the conditional probability $p_{I|I_H}(I|I_H)$ given I_p can be written as

$$p_{I|I_H}(I|I_H) = \frac{1}{I_H}\frac{z^2}{A_r^{z^2}}\left(\frac{I}{I_H}\right)^{z^2-1}, 0 \le I \le I_H A_r. \tag{22}$$

Remark 2. *In our considerations, we have treated atmospheric turbulence and pointing errors as statistically independent phenomena. Pointing errors, often attributed to building sway, typically exhibit a correlation time in the range of a few seconds, as indicated by previous studies [30]. This correlation time is significantly greater than that of atmospheric turbulence. Given this, it is reasonable to assume independence between atmospheric turbulence and pointing errors.*

Theorem 2. *An approximate analytical PDF expression for the combined effect of cascaded lognormal fading channel and generalized pointing errors in terms of Meijer-G function can be expressed as*

$$p_I(I) = \frac{z^2 I^{z^2-1}}{\left(\frac{m_{I_H} A_r}{\Omega_{I_H}}\right)^{z^2}\Gamma(m_{I_H})} \times G_{1,2}^{2,0}\left(\frac{m_{I_H} I}{A_r \Omega_{I_H}}\Big|_{0, m_{I_H}-z^2}^{1}\right). \tag{23}$$

Proof. Assuming path loss to be unity and substituting (20) and (22) in (21), and simplifying we have

$$\begin{aligned} p_I(I) = \frac{1}{\Gamma(m_{I_H})}\left(\frac{m_{I_H}}{\Omega_{I_H}}\right)^{m_{I_H}} \frac{z^2}{A_r^{z^2}} I^{z^2-1} \\ \times \int_{I/A_r}^{\infty} I_H^{m_{I_H}-z^2-1} e^{-\frac{m_{I_H} I_H}{\Omega_{I_H}}} dI_H. \end{aligned} \tag{24}$$

(24) can be rewritten as

$$\begin{aligned} p_I(I) = \frac{1}{\Gamma(m_{I_H})}\left(\frac{m_{I_H}}{\Omega_{I_H}}\right)^{m_{I_H}} \frac{z^2}{A_r^{z^2}} I^{z^2-1} \\ \times \left[\int_{m_{I_H} I/\Omega_{I_H} A_r}^{\infty}\left(\frac{m_{I_H} I_H}{\Omega_{I_H}}\right)^{m_{I_H}-z^2-1} \right. \\ \left. \times e^{-\frac{m_{I_H} I_H}{\Omega_{I_H}}} d\left(\frac{m_{I_H} I_H}{\Omega_{I_H}}\right)\right]\left(\frac{\Omega_{I_H}}{m_{I_H}}\right)^{m_{I_H}-z^2-1} \times \frac{\Omega_{I_H}}{m_{I_H}}. \end{aligned} \tag{25}$$

Denoting $\frac{m_{I_H} I_H}{\Omega_{I_H}} = x$, $m_{I_H} - z^2 = y$, (25) can be written as

$$\begin{aligned} p_I(I) = \frac{1}{\Gamma(m_{I_H})}\left(\frac{m_{I_H}}{\Omega_{I_H}}\right)^{m_{I_H}} \frac{z^2}{A_r^{z^2}} I^{z^2-1} \\ \times \left[\int_{m_{I_H} I/\Omega_{I_H} A_r}^{\infty} x^{y-1}\exp^{-x} dx\right]. \end{aligned} \tag{26}$$

Using the definition of upper incomplete gamma function, i.e., $\Gamma(y) = \int_0^{\infty} x^{y-1} e^{-x} dx$, we have

$$\begin{aligned} p_I(I) = \frac{1}{\Gamma(m_{I_H})}\left(\frac{m_{I_H}}{\Omega_{I_H}}\right)^{m_{I_H}} \frac{z^2}{A_r^{z^2}} I^{z^2-1} \\ \times \Gamma\left(m_{I_H} - z^2, \frac{m_{I_H} I_H}{A_r \Omega_{I_H}}\right). \end{aligned} \tag{27}$$

Expressing gamma function in terms of Meiger-G function we get (23). □

D. Statistics of the cascaded gamma-gamma channel model with pointing error

Theorem 3. *A closed form PDF expression for the combined effect of cascaded gamma-gamma fading channel and generalized pointing errors is given as*

$$p_I(I) = \Upsilon \frac{z^2}{A_r} G_{1,2N+1}^{2N+1,0} \times \left(\left(\prod_{n=1}^{N}(\alpha_n \beta_n)\right)\frac{I}{A_r}\Big| z^2 - 1, \Xi\right). \tag{28}$$

$$p_I(I) = \Upsilon \frac{z^2 I^{z^2-1}}{A_r^{z^2}} \times \int_{I/A_r}^{\infty} dI G_{0,2N}^{2N,0}\left(\left(\prod_{n=1}^{N}(\alpha_n \beta_n)\right) I\Big|_{\Xi}^{\cdots}\right)\left(\frac{1}{I}\right)^{z^2}. \tag{29}$$

Proof. Assuming path loss to be unity and substituting (8) and (22) in (21) we get (29). Then using equation (07.34.21.0085.01) of [49] and simplifying we arrive at equation (28). □

IV. Error Rate Performance Analysis of Cascaded VFSO Link

In this section, we take a HAP based VFSO link with intensity modulation and direct detection. We have assumed on-off keying signaling technique. The BER is given by

$$BER = p(e|0) = p(e|1) = \frac{1}{2}\operatorname{erfc}\left(\frac{P_t I}{\sqrt{2}\sigma_n}\right) \tag{30}$$

where $\mathrm{erfc}(\cdot)$ is the complementary error function. By averaging BER in (30) over the PDF of I gives

$$\overline{BER} = \frac{1}{2}\int_0^\infty p_I(I)\,\mathrm{erfc}\left(\frac{P_t I}{\sqrt{2}\sigma_n}\right) dI. \tag{31}$$

We use (31) to obtain closed-form average BER expressions for cascaded lognormal and cascaded gamma-gamma channels with generalized pointing errors which is given in the following subsection.

A. BER over cascaded lognormal channel with pointing error

Theorem 4. *The expression for average BER of a cascaded lognormal vertical channel with generalized pointing error is given by* (32).

Proof. By replacing (23) in (31), we obtain equation (33). By expressing the complementary error function in terms of the Meijer G-function we have (34). The first term in (34) can be split as $\int_0^\infty f(x)dx = \int_0^1 f(x)dx + \int_1^\infty f(x)dx$. The integration of the first term is solved using (07.34.21.0084.01) and (07.34.21.0085.01) from [49]. On the other hand, the second term in (34) is evaluated using the integration of two product Meijer G-functions, as given by (07.34.21.0013.01) from [49]. Then, we apply the property of Meijer G-functions, given by equation (4.257) in [49], to perform further mathematical manipulations and arrive at (32). □

B. BER over cascaded gamma-gamma channel with pointing error

Theorem 5. *The expression for average BER of a cascaded gamma-gamma VFSO link suffering from pointing error is given by* (35).

Proof. After substituting (28) in (31), we obtain (36). Using Meijer G-function for expressing complementary error function we get (36) as (37). Next, we split the first term in (37) into two separate integrations: $\int_0^\infty f(x)dx = \int_0^1 f(x)dx + \int_1^\infty f(x)dx$. The integration of the first term is then solved using (07.34.21.0084.01) and (07.34.21.0085.01) from [49]. Similarly, the second term in (37) is addressed by performing the integration of product of two Meijer G-functions, as given by (07.34.21.0013.01) from [49]. Using Eq. (4.257) of [49] for further simplifications lead to the final form of (35). □

C. Thickness calculation of the cascaded layers

We consider HAP stations located at high altitudes, and discuss the appropriate thickness of the layers to be used in the modeling. The scintillation index is a crucial parameter in characterizing the strength of atmospheric turbulence, which is required for calculating PDF, as described in the previous sections. Assuming a plane optical beam, the scintillation index for every layer can be expressed as [13]:

$$\sigma_{I_n}^2 = 8\pi^2 k_0^2 d_n \times \int_0^1\int_0^\infty \kappa\Phi_{n_k}(\kappa)\left(1 - cos\left[d_n\frac{\kappa^2\zeta}{k_o}\right]\right) d\kappa d\zeta \tag{38}$$

where κ is the magnitude of the spatial frequency and $k_0 = \frac{2\pi}{\lambda}$ is the wave number, λ denotes the wavelength. $\Phi_{n_k}(\kappa)$ in (38) represents the spatial power spectrum model for the fluctuations in atmospheric refractive index for the n^{th} layer. In our study we have used the *modified atmospheric spectrum* which is given by

$$\Phi_{n_k}(\kappa) = 0.033C_n^2\left[1 + 1.802\left(\frac{\kappa}{\kappa_l}\right) - 0.254\left(\frac{\kappa}{\kappa_l}\right)^{7/6}\right] \times \frac{\exp(-\kappa^2/\kappa_l^2)}{(\kappa^2+\kappa_0^2)^{11/6}}, 0 \le \kappa < \infty; \kappa_l = 3.3/l_0 \tag{39}$$

where, $\kappa_0 = 2\pi/L_0$.

It is notable that, most of the theoretical studies of optical wave propagation are based on Kolmogorov, Von-Karman, Tatarskii spectrum models because of mathematical convenience. In a strict sense, these spectrum models accurately depict the behavior of turbulence only within the inertial range. Only the modified atmospheric spectrum features the high wave number rise prior to the dissipation range that is of particular importance in scintillation studies.

The presence of spectral bump produces enhanced scintillation. The calculation of scintillation index based on modified atmospheric spectrum for both weak and strong fluctuation regime is given in Appendix B. The selection of each layer's thickness d_n should ensure that the alteration in the log-amplitude variance of the beam within that specific layer

$$\overline{BER_{LN}} = \frac{2^{m_{I_H}-2}}{\sqrt{\pi}}\left(\frac{m_{I_H}}{A_r\Omega_{I_H}}\right)^{-z^2} G_{5,4}^{1,5}\left(\frac{\frac{P_t^2}{2\sigma_n^2}}{\left(\frac{m_{I_H}}{A_r\Omega_{I_H}}\right)^2.2^2}\Big|^{1,\frac{1-z^2}{2},\frac{2-z^2}{2},\frac{z^2-m}{2},\frac{1+z^2-m}{2}}_{\frac{1}{2},\frac{-z^2}{2},\frac{-z^2}{2},\frac{1-z^2}{2}}\right). \tag{32}$$

$$\overline{BER_{LN}} = \frac{1}{2}\int_0^\infty \frac{z^2 I^{z^2-1}}{\left(\frac{m_{I_H}A_r}{\Omega_{I_H}}\right)^{z^2}\Gamma(m_{I_H})}\cdot G_{1,2}^{2,0}\left(\frac{m_{I_H}I}{A_r\Omega_{I_H}}\Big|^{1}_{0,m_{I_H}-z^2}\right) erfc\left(\frac{P_t I}{\sqrt{2}\sigma_n}\right) dI. \tag{33}$$

$$\overline{BER_{LN}} = \frac{1}{2}\frac{z^2}{\left(\frac{m_{I_H}A_r}{\Omega_{I_H}}\right)^{z^2}\Gamma(m_{I_H})}\left[\int_0^\infty I^{z^2-1}G_{1,2}^{2,0}(\aleph)\right] - \frac{1}{\sqrt{\pi}}\left[\int_0^\infty I^{z^2-1}G_{1,2}^{2,0}(\aleph)\,G_{1,2}^{1,1}\left(\frac{P_t^2}{2\sigma_n^2}I^2\Big|^{1}_{\frac{1}{2},0}\right) dI\right]. \tag{34}$$

where, $\aleph = \frac{m_{I_H}I}{A_r\Omega_{I_H}}\Big|^{1}_{0,m_{I_H}-z^2}$.

remains below a predetermined threshold, denoted as ϵ. The log-irradiance variance, $\sigma^2_{x_n}$, is connected to the scintillation index, $\sigma^2_{I_n}$, through the relationship outlined in (2) for weak turbulence and (7) for regions characterized by strong turbulence. The procedure begins with the calculation of $\sigma^2_{I_0}$ at ground level and $\sigma^2_{I_{\Delta d}}$ at a height of $\Delta d = 50\ m$ from ground level. Subsequently, the absolute error between $\sigma^2_{I_0}$ and $\sigma^2_{I_{\Delta d}}$ is computed. If the absolute error falls below the predefined threshold ϵ, the computation of $\sigma^2_{I_{\Delta d}}$ continues by adding $50\ m$ to the previous Δd, and this process is repeated until the absolute error surpasses the threshold value. The value of Δd at this point indicates the current layer's thickness. These steps are reiterated till we reach HAP height d_H under consideration. The detailed procedure for determining the thickness of each layer is outlined in Algorithm 1. The subsequent section presents the variation in log-irradiance values concerning both changes in height and variations in the refractive index structure parameter (C_n^2) as one ascends from ground level.

Algorithm 1: No. of layers and their thickness

Input $\sigma^2_{I_0}$, Δd , d_H and ϵ;
Output d_n and N;
Initialize $N = 1$, $d_n = [\,]$;
Set $i = 1$, $d = 0$;
Set $\sigma^2_{I_{ref}} = \sigma^2_{I_0}$;
Set $d(i) = d(i-1) + \Delta d$;
$y \leftarrow 1$;
$X \leftarrow x$;
$N \leftarrow n$;
while $d(i) \leq d_H$ **do**
  Find $\sigma^2_{I_{\Delta d}}$ using eq. (2) and eq. (7)
  if $\left|\frac{\sigma^2_{I_{\Delta d}} - \sigma^2_{I_{ref}}}{\sigma^2_{I_{ref}}}\right| \leq \epsilon$ **then**
    $i \leftarrow i + 1$;
    $d(i) \leftarrow d(i-1) + \Delta d$
  else
    if $\left|\frac{\sigma^2_{I_{\Delta d}} - \sigma^2_{I_{ref}}}{\sigma^2_{I_{ref}}}\right| > \epsilon$ **then**
      $\sigma^2_{I_{ref}} \leftarrow \sigma^2_{I_{\Delta d}}$;
      $N \leftarrow N + 1$;
      $d_n = [d_n, d_i]$;
      $i \leftarrow i + 1$;
    end
  end
  $d(i) \leftarrow d(i-1) + \Delta d$;
end

V. Numerical Results and Discussion

We provide numerical results for our cascaded VFSO channel model expressions for both weak and strong atmospheric turbulence in this section. We validate our expressions using correlated phase screen simulated data points for VFSO channel. Next, we present numerical results for the derived BER expressions. To validate the correctness of our calculations we run 10^5 Monte-Carlo simulations. The main challenge in our simulations is to generate precise fading coefficients that have the desired value of $\sigma^2_{x_n}$ for the lognormal turbulence channel, as well as the desired values of α_n and β_n for the gamma-gamma turbulence channel. α_n and β_n are linked to the scintillation index denoted as $\sigma^2_{I_n}$, as explained in Sections II.A and II.B. We compute $\sigma^2_{x_n}$ for varying heights and turbulence strengths C_n^2. The change in $\sigma^2_{x_n}$ with increasing turbulence strength and with changing vertical heights are given in Fig. 5. *The impact of increasing height and varying turbulence strength C_n^2 on $\sigma^2_{x_n}$ is quite evident from Fig. 5 which highlights the importance of incorporating such variations in the VFSO channel model.*

For correlated phase screen simulation model we have considered a plane optical beam propagating in atmospheric turbulence. Numerical simulation values that define the physical conditions are the ratio l_0/R_F and $\sigma^2_{I_n}$, as described in [46]. Here, $l_0 = 0.5R_F$ represents the inner scale of turbulence, and R_F is the scale size of the Fresnel zone. $R_F = \sqrt{H/k}$, where H is the vertical height and $k = 2\pi/\lambda$. The other simulation parameters are $\lambda = 1550nm$, rms windspeed = $21m/s$, C_n^2 is computed using $H - V_{5/7}$ model [42] and $A = 1.7 \times 10^{-14} m^{-2/3}$ is the nominal value of C_n^2 at ground level. In addition to the refractive index, it is essential to specify the sizes of the turbulent eddies constituting the upper and lower boundaries of the turbulent atmosphere. To model L_0 as a function of H, the empirical Coulman-Vernin profile is utilised [43]. The derived numerical results using these parameters are given in following subsections.

A. Cascaded channel model PDF simulation using correlated phase screens

Flatté et al. (1994) [46] conducted numerical simulations to calculate PDF of a plane optical beam travelling in

$$\overline{BER_{GG}} = -\partial^{-1} \frac{2^{\left(\sum_{i=1}^{N}(\alpha_i+\beta_i)\right)-2N-1}}{\left[\frac{\prod_{N=1}^{N}(\alpha_n\beta_n)}{A_r}\right]\sqrt{\pi}(\pi)^N} G^{4N+3,1}_{4,4N+3}\left(\frac{\left(\frac{\prod_{N=1}^{N}(\alpha_n\beta_n)}{A_r}\right)^2}{\frac{P_t^2}{2\sigma_n^2}2^{4N}}\Big|_{0,\,\frac{z^2+1}{2},\,\frac{z^2}{2},\,\frac{\alpha_1+1}{2},\ldots,\frac{\alpha_1}{2},\ldots,\frac{\alpha_n}{2},\,\frac{\beta_1+1}{2},\ldots,\frac{\beta_1}{2},\ldots,\frac{\beta_n}{2}}^{\frac{1}{2},\,\frac{2-z^2}{2},\,\frac{1+z^2}{2},\,1}\right). \tag{35}$$

$$\overline{BER_{GG}} = \frac{1}{2}\int_0^\infty \Upsilon \frac{z^2}{A_r} G^{2N+1,0}_{1,2N+1}\left(\left(\prod_{n=1}^{N}(\alpha_n\beta_n)\right)\frac{I}{A_r}\Big| z^2 \atop z^2-1,\Xi\right)\operatorname{erfc}\left(\frac{P_t I}{\sqrt{2}\sigma_n}\right) dI. \tag{36}$$

$$\overline{BER_{GG}} = \frac{1}{2}\Upsilon\frac{z^2}{A_r}\int_0^\infty G^{2N+1,0}_{1,2N+1}\left(\frac{\partial I}{A_r}\Big| z^2 \atop z^2-1,\Xi\right) dI - \frac{1}{2\sqrt{\pi}}\Upsilon\frac{z^2}{A_r}\int_0^\infty G^{2N+1,0}_{1,2N+1}\left(\frac{\partial I}{A_r}\Big| z^2 \atop z^2-1,\Xi\right) G^{1,1}_{1,2}\left(\frac{P_t^2}{2\sigma_n^2}I^2\Big|_{\frac{1}{2},0}^{1}\right) dI. \tag{37}$$

where, $\partial = \left(\prod_{n=1}^{N}(\alpha_n\beta_n)\right)$.

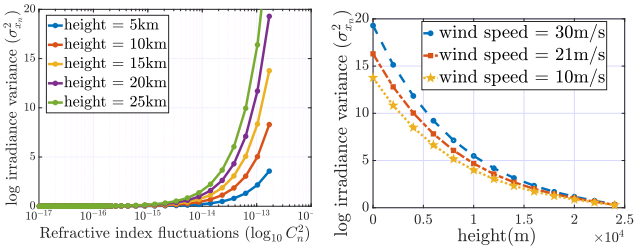

Figure 5: Variation in log-irradiance values with changes in height and variations in the refractive index structure parameter as one ascends from ground level.

homogeneous and isotropic turbulence in weak fluctuation regime. Similarly, Hill et al. (1997) [50] performed numerical simulations of a spherical optical beam travelling in homogeneous and isotropic turbulence, leading to PDF data for log-irradiance fluctuations in moderate-to-strong fluctuation regimes. Based on these published results Safi et al. [51] conducted research on analytical channel model and link design optimization for ground-to-HAP FSO link. Considering these FSO channel models as a benchmark, we compare our proposed cascaded channel model with the log-irradiance PDF plots by numerically simulating the existing lognormal and gamma-gamma PDFs in these literatures [46], [50], [51]. We denote the existing PDFs reported in these literatures as *conventional lognormal* and *conventional gamma gamma PDF*. Our simulation results encompasses various fading conditions, ranging from weak turbulence regions to the saturation regions specified by the rytov variance, $\sigma^2_{I_n}$. Following a similar approach as given by Flatté et al. (1994), we simulate the PDF values as a function of $(\ln I - < \ln I >)/\sigma$, where the mean value of log-irradiance is expressed as $< \ln I >$ and $\sigma = \sqrt{\sigma^2_{\ln I}}$ denotes the rms value of $\ln I$. The simulation results are displayed in this manner for better comparison with the existing PDFs and to highlight their key characteristics.

In Fig. 6 (a), we consider an optical beam travelling in weak irradiance fluctuations. We plot the PDF graph on a linear scale to highlight the deviation of cascaded PDF from that calculated using lognormal PDF used in the literature so far. We have considered a vertical link of 10 km. We have also shown that the correlated phase screen simulated data points agree more with the cascaded PDF as compared to conventional lognormal PDF used to characterize weak turbulence regime. We see that the conventional PDF tend to underestimate the peak fluctuations in irradiance under weak turbulence regions. Fig. 6 (b) shows the same plot on logarithmic scale. Fig. 6 (c , d) shows the log-irradiance value for a vertical beam at 15 km and 25 km vertical height respectively. The conventional lognormal PDF tend to deviate more especially at the tails from the simulated data points but the cascaded lognormal channel model is in agreement with the simulation data points.

In Fig. 7, we consider an optical beam travelling in strong irradiance fluctuations. The PDF graph is plotted on a linear scale to emphasize the differences between the cascaded PDF and the conventional gamma-gamma PDF. Here also, we have considered a vertical link of 10 km. As can be seen from the results that in strong fluctuation regime also the correlated phase screen simulated data points align better with the cascaded PDF compared to the conventional gamma-gamma PDF, particularly in predicting the peak irradiance fluctuations. Fig. 7 (b) presents the same plot but on a logarithmic scale for better visualization. Further, in Fig. 7 (c, d) the log-irradiance values are shown for a vertical beam at heights of 15 km and 25 km, respectively. It is evident that the conventional gamma-gamma PDF tends to deviate more, especially at the tails, from the simulated data points. In contrast, the cascaded gamma-gamma channel model demonstrates a better agreement with the simulation data points.

Remark 3. *The linear plot results reveal that in the weak fluctuation regime, the conventional lognormal PDF tends to underestimate peak fluctuations by about* 14%*. Conversely, in the strong turbulence regions, the conventional gamma-gamma PDF tends to overestimate peak irradiance fluctuations by about* 17%*. These mismatches highlights how the conventional channel modeling approach, which employs turbulence averaging throughout the propagation distance, tends to over/under estimate irradiance fluctuations of a vertical traveling beam facing varying turbulence strengths.*

To summarize, we present below some interesting takeaways about the newly developed concatenated channel model PDF of the received intensity of the laser beam propagating through vertical turbulence:

1) From Fig. 6 (a), it is observed that the conventional lognormal PDF underestimate the peak of the received irradiance PDF. It also underestimated the irradiance behavior in the tails as compared with correlated phase screen data as can be seen in Fig. 6 (b). Underestimation of the tails in the PDF has significant implications for a HAP based FSO link because the fade probabilities are predominantly determined at the tails of the received optical irradiance PDF.
2) As the vertical propagation distances increases, the deviation of the conventional lognormal PDF from the simulated data points becomes more apparent as can be seen from Fig. 6 (c, d). It is interesting to note that the cascaded lognormal PDF agrees well with the simulation results even after increasing the distance of vertical propagation of laser beam through turbulent atmosphere.
3) As the laser beam encounters strong turbulence the proposed cascaded gamma-gamma PDF matches the correlated phase screen data points for almost all abscissa values as can be seen in Fig. 7 (a). The conventional gamma-gamma channel model deviates from the simulated data points in the extreme tails particularly for abscissa values less than -1 shown in Fig. 7 (b).
4) The disparity between the conventional gamma-gamma PDF and the simulated data points becomes quite evident as vertical height increases shown in Fig. 7 (c, d). In contrast, the cascaded gamma-gamma PDF agrees well with the simulation results for all heights.
5) The authors would like to bring attention of the readers to the fact that the cascaded distribution model used in this subsection is intentionally constrained to have

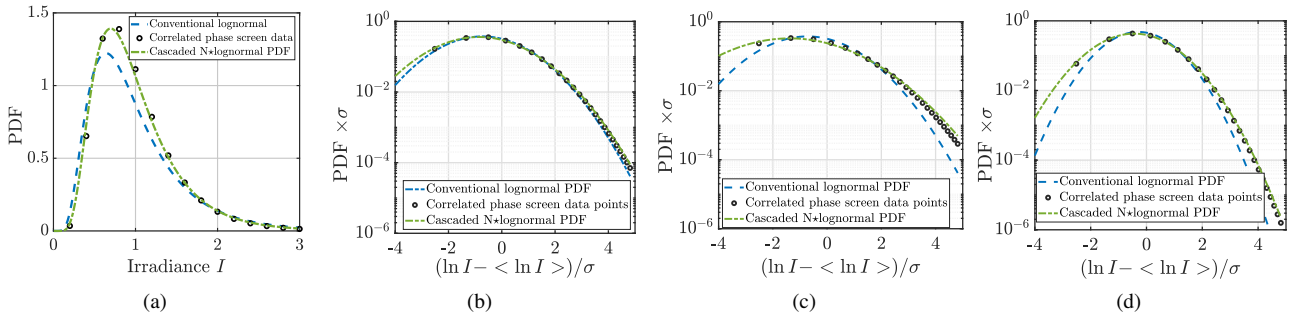

Figure 6: Scaled log-irradiance PDF for a plane optical beam travelling in weak turbulence regions in vertical FSO link configuration ($\epsilon = 10\%$ and $l_o/R_F = 0.5$) (a) Vertical link distance = 10 km (Linear Scale) (b) Vertical link distance = 10 km (logarithmic scale) (c) Vertical link distance = 15 km (logarithmic scale) (d) Vertical link distance = 25 km (logarithmic scale).

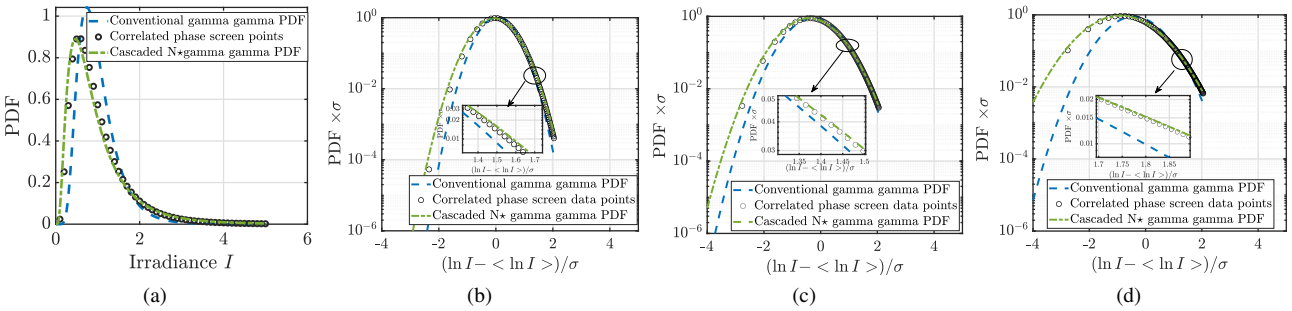

Figure 7: Scaled log-irradiance PDF for a plane optical beam traveling in very strong turbulence regions in vertical FSO link configuration ($\epsilon = 10\%$ and $l_o/R_F = 0.5$. (a) Vertical link distance = 10 km (Linear Scale) (b) Vertical link distance = 10 km (logarithmic scale) (c) Vertical link distance = 15 km (logarithmic scale) (d) Vertical link distance = 25 km (logarithmic scale).

a limited number of layers, restricted to a 10% variance change within the layer ($\epsilon = 10\%$). This limitation aims to maintain the tractability of the developed PDFs by minimizing the complexity of the mathematical expressions along with maintaining high accuracy.

To substantiate the applicability of the proposed PDF channel models for practical VFSO scenarios, we proceed to illustrate the error performance of HAP based optical wireless communication link in the following subsection. For the sake of completeness of the study, we also present the effect of increasing and decreasing the number of cascaded layers on the error performance by taking different threshold value (ϵ) in the next subsection.

B. BER performance of proposed cascaded channel model

In Fig. 8 (a) we illustrate the BER performance of a VFSO link propagating in weak turbulence regime. In this setup, the transmitter is positioned at ground, while the receiver is located 25 km away and the beam is traveling through a region of weak turbulence. The BER expression derived from the cascaded lognormal PDF is plotted alongside the results obtained from CPS simulations. In modeling the vertical link, we consider two, four and seven independent layers, each with varying thickness by changing the threshold value ϵ proposed in Algorithm 1 to 50%, 30% and 10% respectively. Our results indicate a close alignment between the derived expression and the simulated BER performance across different Signal-to-Noise Ratio (SNR) values. We also simulate the BER performance of a VFSO beam unaffected by turbulence for reference. Notably, turbulence introduces a substantial degradation of approximately 20 dB in the HAP based VFSO link performance in weak turbulence regions. For additional benchmarking, we incorporate the BER performance of an idealized VFSO beam experiencing the same level of turbulence for the entire propagation distance. For modeling this propagation channel, the constant σ_H^2 is derived by averaging temperature and refractive index fluctuation values for entire propagation distance transmission range. However, it is observed that this simplified approach underestimates actual BER values. Moreover, the disparity in performance of the actual and hypothetical scenarios widens as the number of layers to model the vertical channel increases. In Fig. 8 (b), we illustrate the combined impact of turbulence and pointing errors on the VFSO link, revealing an additional degradation of about 10 dB.

Remark 4. *In Fig. 8 (a), it is evident that the newly developed expressions demonstrate an approximate accuracy of 2 dB for a BER of 10^{-4} in HAP-based optical networks under*

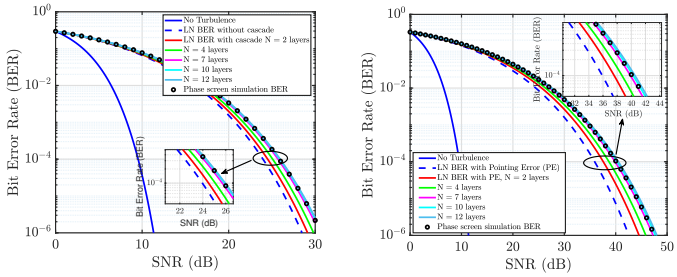

(a) (b)

Figure 8: (a) Average BER performance of cascaded lognormal (LN) turbulence channel by considering different number of layers. Correlated phase screen based simulation results are denoted by circles. (b) Average BER performance of cascaded lognormal turbulence channel by considering composite effect of turbulence and pointing errors.

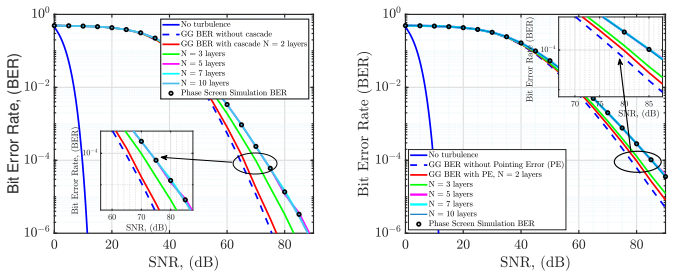

(a) (b)

Figure 9: (a) Average BER performance of concatenated gamma-gamma (GG) turbulence channel. Correlated phase screen based simulation results are denoted by circles. (b) Average BER performance of cascaded GG turbulence channel by considering composite effect of turbulence and pointing errors.

conditions of weak turbulence, surpassing existing competitive models. This accuracy margin expands to 4 *dB when accounting for pointing errors in HAP-based optical networks, as illustrated in Fig. 8 (b).*

Remark 5. *The simulation results show that further increasing the number of layers to ten and twelve has no significant impact in the calculation of BER expressions. It is observed that as long as change in variance between the layers is less than ten percent i.e.* $\epsilon \leq 10\%$ *the average BER comes out to be same and close to simulated BER data points.*

Fig. 9 (a) presents the BER for a VFSO link experiencing strong turbulence conditions. The impact of wind is more prevalent near the ground surface resulting in strong turbulence levels particularly in troposphere. Hence, for this turbulent channel we have considered a vertical link of 10 km and the beam is travelling through strong turbulence. The BER expression derived using the cascaded gamma-gamma PDF is plotted alongside the results obtained from CPS simulations. For modeling the vertical link, multiple independent layers (two, three, and five) are considered, each with varying thickness and threshold value ϵ again set to 50%, 30% and 10% respectively. The results indicate close match between the derived expression and the simulated BER performance. As a benchmark, a VFSO link propagating in vacuum (experiencing no turbulence) is simulated and its BER performance is observed. It can be seen that turbulence introduces a significant degradation in the VFSO link performance in strong turbulence scenario. Additionally, a hypothetical VFSO beam experiencing the same level of turbulence throughout the transmission range is simulated for comparison. Note also that this simplified assumption leads to an underestimation of the actual BER values. Additionally, the performance disparity between the actual and hypothetical scenarios grows with an increase in the number of layers in the vertical link. Interestingly, further increasing the number of layers beyond five to seven or ten does not significantly alter the BER expressions. Here also, as long as the variance change between the layers remains within ten percent ($\epsilon \leq 10\%$), the average BER remains close to the simulated data points. In Fig. 9 (b), the combined effect of turbulence and pointing errors on the VFSO link is shown. We notice that pointing errors introduce an additional degradation of about more than 10 dB in the VFSO link.

Remark 6. *In both Fig. 9 (a) and (b), it is apparent that the newly developed expressions demonstrate an approximate accuracy of* 8 *dB for a BER of* 10^{-4} *in HAP-based optical networks under conditions of strong turbulence, as compared to existing competitive models. Same level of accuracy margin is achieved after accounting pointing errors in HAP-based optical networks under strong turbulence regions.*

VI. Conclusion

In this paper, a novel vertical channel model for HAP based FSO network is presented for both weak and strong atmospheric turbulence regime. The VFSO channel is broken into multiple layers to account for variable turbulence strength. The fading coefficients for these layers are treated as independent and non identically distributed lognormal and gamma-gamma random variables, depending on the turbulence strength. To analyze the performance of the vertical FSO networks, closed-form expressions have been derived for the cascaded channel PDF with pointing error. Then the overall channel model has been utilized to derive the BER performance of the vertical links, and the results have been validated using correlated phase screen simulation data. Additionally, we have conducted a benchmark comparison with a hypothetical vertical link assuming constant turbulent strength, revealing that this simplistic constant-turbulence-strength assumption leads to inaccurate BER estimations, resulting in its underestimation across different SNR regions. The use of the proposed cascaded channel models proves to be more effective in capturing the complex nature of the VFSO link, providing more accurate BER performance predictions for HAP-based optical networks.

$$p_{I_H}(I_H) = \frac{\alpha_1\alpha_2\beta_1\beta_2}{\Gamma(\alpha_1)\Gamma(\alpha_2)\Gamma(\beta_1)\Gamma(\beta_2)} \int_0^\infty I_1^{-1} G_{0,2}^{2,0}\left(\alpha_2\beta_2\frac{I_H}{I_1}\Big|_{\beta_2-1,\alpha_2-1}^{\cdots}\right) G_{0,2}^{2,0}\left(\alpha_1\beta_1 I_1\Big|_{\beta_1-1,\alpha_1-1}^{\cdots}\right) dI_1. \quad (42)$$

$$p_{I_H}(I_H) = \frac{\alpha_1^2\alpha_2\beta_1^2\beta_2}{\Gamma(\alpha_1)\Gamma(\alpha_2)\Gamma(\beta_1)\Gamma(\beta_2)} \int_0^\infty G_{0,2}^{2,0}\left(\frac{I_1}{\alpha_2\beta_2 I_H}\Big|^{2-\beta_2, 2-\alpha_2}_{\cdots}\right) G_{0,2}^{2,0}\left(\alpha_1\beta_1 I_1\Big|_{\beta_1-2,\alpha_1-2}^{\cdots}\right) dI_1. \quad (43)$$

$$p_{I_H}(I_H) = \frac{\alpha_1\alpha_2\beta_1\beta_2}{\Gamma(\alpha_1)\Gamma(\alpha_2)\Gamma(\beta_1)\Gamma(\beta_2)} G_{4,0}^{0,4}\left(\alpha_1\alpha_2\beta_1\beta_2 I_H\Big|_{\alpha-1,\alpha_2-1,\beta_1-1\beta_2-1}^{\cdots}\right). \quad (44)$$

$$\sigma_{I_n}^2 = 3.86\sigma_R^2\left((1+\frac{1}{Q_l^2})^{\frac{11}{2}}\left(\sin\left(\frac{11}{6}\tan^{-1}Q_l\right) + \frac{1.507}{(1+Q_l^2)^{\frac{1}{4}}}\sin\left(\frac{4}{3}\tan^{-1}Q_l\right) - \frac{0.273}{(1+Q_l^2)^{7/24}}\sin\left(\frac{5}{4}\tan^{-1}Q_l\right)\right) - \frac{3.50}{Q_l^{5/6}}\right). \quad (45)$$

VII. APPENDICES

A. Proof of theorem 1

Initially, we take two random variables, which are both gamma-gamma distributed. The PDF of $I_H = I_1 \times I_2$ is given by

$$p_{I_H}(I_H) = \int_{-\infty}^{\infty} f_{I_1}(I_1) f_{I_2}\left(\frac{I_H}{I_1}\right)\frac{1}{|I_1|} dI_1. \quad (40)$$

We use (03.04.26.0009.01) of [49] to represent $K_\nu(\cdot)$ in (4) through Meijer's G-function and simplify the resulting PDF expression mentioned in (4) to get

$$p_{I_n}(I_n) = \frac{\alpha_n\beta_n}{\Gamma(\alpha_n)\Gamma(\beta_n)} G_{0,2}^{2,0}\left(\alpha_n\beta_n I_n\Big|_{\alpha_n-1,\beta_n-1}^{\cdots}\right). \quad (41)$$

Substituting (41) in (40) yields (42). Solving Meijer's G-function gives (43), which can be rewritten as (44) using Meijer's G-function properties. Applying mathematical induction theory on (4) and (44) we get (8).

B. Scintillation Index : Plane Wave

In weak fluctuation regime, putting (39) in (38) gives (45). Here, $Q_l = \frac{d_n\kappa_l^2}{k} = \frac{10.89 d_n}{k l_0^2}; \sigma_R^2 = 1.23 C_n^2 k^{7/6} d_n^{11/6}$. In strong fluctuation regime, putting (39) in (38) gives $\sigma_{I_n}^2 = \exp\left[\sigma_{lnX}^2(l_0) - \sigma_{lnX}^2(L_0) + \frac{0.51\sigma_{PL}^2}{(1+0.69\sigma_{pl}^{12/5})}^{5/6}\right] - 1$. The expressions for $\sigma_{lnX}^2(l_0)$ and $\sigma_{lnX}^2(L_0)$ can be found in Appendix III of [13] and $Q_0 = \frac{d_n\kappa_0}{k}$.

REFERENCES

[1] N. Tiwari, S. De, and S. Dharmaraja, "Modeling of Channel Asymmetry in HAP-based Optical Wireless Communications," in *Proc. NCC*, Feb 2023, pp. 1–6.

[2] X. Cao, P. Yang, M. Alzenad, X. Xi, D. Wu, and H. Yanikomeroglu, "Airborne Communication Networks: A Survey," *IEEE J. Sel. Areas Commun*, vol. 36, no. 9, pp. 1907–1926, Sep 2018.

[3] E. Zedini, Y. Ata, and M.-S. Alouini, "Improving Performance of Integrated Ground-HAPS FSO Communication Links With MIMO Application," *IEEE Photon. J.*, vol. 16, no. 2, pp. 1–14, Apr 2024.

[4] G. Xu, Z. Zhao, Z. Song, Q. Zhang, and B. Ai, "Symbol Error Analysis for Integrated Satellite-Terrestrial Relay Networks with Non-orthogonal Multiple Access Under Hardware Impairments," *IEEE Trans. on Wirel Commun.*, pp. 1–1, May 2024.

[5] D. Grace and M. Mohorcic, *Broadband communications via high altitude platforms*. John Wiley & Sons, Aug 2011.

[6] M. Sharma, D. Chadha, and V. Chandra, "High-altitude platform for free-space optical communication: Performance evaluation and reliability analysis," *J. Opt. Commun. Netw.*, vol. 8, no. 8, pp. 600–609, Aug 2016.

[7] Facebook, "Internet.org by Facebook," [online] https://internet.org/.

[8] Google, "Project Loon," [online] https://x.company/loon/.

[9] I. Toselli, "Introducing the concept of anisotropy at different scales for modeling optical turbulence," *J. Opt. Soc. Am. A, Optica Publishing Group*, vol. 31, no. 8, pp. 1868–1875, Jul 2014.

[10] M. T. Nguyen, V. Mai, and H. Kim, "Time-Efficient Simulation of Free-Space Optical Communication Systems Under Atmospheric Turbulence, Pointing Error, and Angle-of-Arrival Fluctuations," *IEEE Photon. J.*, vol. 15, no. 6, pp. 1–9, Dec 2023.

[11] X. Li, Y. Li, X. Song, L. Shao, and H. Li, "RIS assisted UAV for Weather-Dependent Satellite Terrestrial Integrated Network With Hybrid FSO/RF Systems," *IEEE Photon. J.*, vol. 15, no. 5, pp. 1–17, Oct 2023.

[12] W. Guo, Y. Zhan, T. A. Tsiftsis, and L. Yang, "Performance and Channel Modeling Optimization for Hovering UAV-Assisted FSO Links," *J. Light. Technol.*, vol. 40, no. 15, pp. 4999–5012, May 2022.

[13] L. C. Andrews and R. L. Phillips, "Laser beam propagation through random media," *Laser Beam Propagation Through Random Media: Second Edition*, Sep 2005.

[14] F. Yang, J. Cheng, and T. A. Tsiftsis, "Free-Space Optical Communication with Nonzero Boresight Pointing Errors," *IEEE Trans. Commun.*, vol. 62, no. 2, pp. 713–725, Feb 2014.

[15] I. S. Ansari, M.-S. Alouini, and J. Cheng, "Ergodic Capacity Analysis of Free-Space Optical Links With Nonzero Boresight Pointing Errors," *IEEE Trans. Wireless Commun.*, vol. 14, no. 8, pp. 4248–4264, Aug 2015.

[16] Y. Ata and M.-S. Alouini, "Performance of Integrated Ground-Air-Space FSO Links Over Various Turbulent Environments," *IEEE Photon. J.*, vol. 14, no. 6, pp. 1–16, Dec 2022.

[17] X. Zhu and J. Kahn, "Free-space optical communication through atmospheric turbulence channels," *IEEE Trans. Commun.*, vol. 50, no. 8, pp. 1293–1300, Aug 2002.

[18] O. S. Badarneh, F. E. Bouanani, F. S. Almehmadi, and H. S. Silva, "FSO Communications Over Doubly Inverted Gamma-Gamma Turbulence Channels With Nonzero-Boresight Pointing Errors," *IEEE Wirel. Commun. Lett.*, vol. 12, no. 10, pp. 1761–1765, Oct 2023.

[19] M. Miao and X. Li, "Performance Analysis of FSO Systems Over a Lognormal-Rician Turbulence Channel With Generalized Pointing Errors," *IEEE J. Light. Technol.*, vol. 40, no. 13, pp. 4206–4216, Jul 2022.

[20] I. S. Ansari, F. Yilmaz, and M.-S. Alouini, "Performance Analysis of Free-Space Optical Links Over Málaga ($\mathcal{M}$) Turbulence Channels With Pointing Errors," *IEEE Trans. Wireless Commun.*, vol. 15, no. 1, pp. 91–102, Jan 2016.

[21] A. A. Ibrahim, S. O. Ata, and L. Durak-Ata, "Performance of FSO Communication Systems Employing Alamouti-Type Space-Time Encoding Over Málaga Channels With Pointing Errors," *IEEE Photon. J.*, vol. 14, no. 1, pp. 1–8, Feb 2022.

[22] L. Qu, G. Xu, Z. Zeng, N. Zhang, and Q. Zhang, "UAV-Assisted RF/FSO Relay System for Space-Air-Ground Integrated Network: A Performance Analysis," *IEEE Trans. Wirel. Commun.*, vol. 21, no. 8, pp. 6211–6225, Aug 2022.

[23] Y. Lou, J. Cheng, D. Nie, and G. Qiao, "Performance of Vertical Underwater Wireless Optical Communications With Cascaded Layered Modeling," *IEEE Trans. Veh. Technol.*, vol. 71, no. 5, pp. 5651–5655, Aug 2022.

[24] M. Elamassie and M. Uysal, "Performance Characterization of Vertical Underwater VLC Links in the Presence of Turbulence," in *Proc. CSNDSP*, Jul 2018, pp. 1–6.

[25] M. T. Dabiri, S. M. S. Sadough, and M. A. Khalighi, "Channel Modeling and Parameter Optimization for Hovering UAV-Based Free-

Space Optical Links," *IEEE J. Sel. Areas Commun.*, vol. 36, no. 9, pp. 2104–2113, Sep 2018.
[26] M. T. Dabiri, S. M. S. Sadough, and I. S. Ansari, "Tractable Optical Channel Modeling Between UAVs," *IEEE Trans. Veh. Technol.*, vol. 68, no. 12, pp. 11 543–11 550, Dec 2019.
[27] P. Beckmann, "Statistical distribution of the amplitude and phase of a multiply scattered field," *J. Res. Natl. Inst. Stand. Technol.*, vol. 3, pp. 231–240, 1962.
[28] W. Gappmair, S. Hranilovic, and E. Leitgeb, "OOK performance for Terrestrial FSO Links in Turbulent Atmosphere with Pointing Errors Modeled by Hoyt Distributions," *IEEE Commun. Lett.*, vol. 15, no. 8, pp. 875–877, Aug 2011.
[29] X. Yu, G. Xu, Q. Zhang, and Z. Song, "Dual-Hop Optical Communication Systems Over Málaga Turbulence Under Pointing Error Impairments With Decode-and-Forward Protocol," *IEEE Photon. J.*, vol. 14, no. 6, pp. 1–15, Dec 2022.
[30] H. G. Sandalidis, T. A. Tsiftsis, and G. K. Karagiannidis, "Optical Wireless Communications With Heterodyne Detection Over Turbulence Channels With Pointing Errors," *IEEE J. Light. Technol.*, vol. 27, no. 20, pp. 4440–4445, Oct 2009.
[31] L.-L. Cao, M. Sheng, M. Feng, and X.-X. Xie, "BER performance of free-space optical communication in strong turbulence with pointing errors," in *Proc. WCSP*, Oct 2012, pp. 1–5.
[32] P. Wang, J. Zhang, L. Guo, T. Shang, T. Cao, R. Wang, and Y. Yang, "Performance analysis for relay-aided multihop BPPM FSO communication system over exponentiated Weibull fading channels with pointing error impairments," *IEEE Photon. J.*, vol. 7, no. 4, pp. 1–20, Aug 2015.
[33] H. AlQuwaiee, I. S. Ansari, and M.-S. Alouini, "On the Performance of Free-Space Optical Communication Systems Over Double Generalized Gamma Channel," *IEEE J. Sel. Areas Commun.*, vol. 33, no. 9, pp. 1829–1840, Sep 2015.
[34] R. Boluda-Ruiz, A. García-Zambrana, B. Castillo-Vázquez, and C. Castillo-Vázquez, "Impact of nonzero boresight pointing error on ergodic capacity of MIMO FSO communication systems," *Opt. Express Optica Publishing Group*, vol. 24, no. 4, pp. 3513–3534, Feb 2016.
[35] E. Zedini, H. Soury, and M.-S. Alouini, "Dual-Hop FSO Transmission Systems Over Gamma–Gamma Turbulence With Pointing Errors," *IEEE Trans. Wirel. Commun.*, vol. 16, no. 2, pp. 784–796, Feb 2017.
[36] R. Boluda-Ruiz, A. García-Zambrana, C. Castillo-Vázquez, and B. Castillo-Vázquez, "Novel approximation of misalignment fading modeled by Beckmann distribution on free-space optical links," *Opt. Express Optica Publishing Group*, vol. 24, no. 20, pp. 22 635–22 649, Oct 2016.
[37] R. Boluda-Ruiz, A. García-Zambrana, C. Castillo-Vázquez, B. Castillo-Vázquez, and S. Hranilovic, "Outage Performance of Exponentiated Weibull FSO Links Under Generalized Pointing Errors," *IEEE J. Light. Technol.*, vol. 35, no. 9, pp. 1605–1613, May 2017.
[38] A. A. Farid and S. Hranilovic, "Outage Capacity Optimization for Free-Space Optical Links With Pointing Errors," *IEEE J. Light. Technol.*, vol. 25, no. 7, pp. 1702–1710, Jul 2007.
[39] S. Yu, J. Ding, Y. Fu, J. Ma, L. Tan, and L. Wang, "Novel approximate and asymptotic expressions of the outage probability and BER in gamma-gamma fading FSO links with generalized pointing errors," *Opt. Commun. Elsevier*, vol. 435, pp. 289–296, Mar 2019.
[40] "The U.S. Standard Atmosphere 1976," [online] https://ntrs.nasa.gov/citations/19770009539.
[41] M. Elamassie and M. Uysal, "Vertical Underwater Visible Light Communication Links: Channel Modeling and Performance Analysis," *IEEE Trans. Wireless Commun.*, vol. 19, no. 10, pp. 6948–6959, Oct 2020.
[42] R. Hufnagel and N. Stanley, "Modulation transfer function associated with image transmission through turbulent media," *J. Opt. Soc. Amer.*, vol. 54, no. 1, pp. 52–61, Jan 1964.
[43] C. Coulman, J. Vernin, Y. Coqueugniot, and J. Caccia, "Outer scale of turbulence appropriate to modeling refractive-index structure profiles," *Appl. Opt.*, vol. 27, no. 1, pp. 155–160, Jan 1988.
[44] W. K. Pratt, *Laser communication systems [by] William K. Pratt*. Wiley New York, Jan 1969.
[45] S. M. Navidpour, M. Uysal, and M. Kavehrad, "BER performance of Free-Space Optical Transmission with Spatial Diversity," *IEEE Trans. Wireless Commun.*, vol. 6, no. 8, pp. 2813–2819, Aug 2007.
[46] S. M. Flatté, C. Bracher, and G.-Y. Wang, "Probability-density functions of irradiance for waves in atmospheric turbulence calculated by numerical simulation," *J. Opt. Soc. Am. A Optica Publishing Group*, vol. 11, no. 7, pp. 2080–2092, Jul 1994.
[47] S. Mukherjee and C. Yardim, "Accurate Computation of Scintillation in Tropospheric Turbulence With Parabolic Wave Equation," *IEEE Trans. Antennas Propag.*, vol. 69, no. 8, pp. 4748–4757, Aug 2021.
[48] I. Kostić, "Analytical approach to performance analysis for channel subject to shadowing and fading," *IEE Proc., Commun. IET*, vol. 152, no. 6, pp. 821–827, Dec 2005.
[49] *Wolfram Research.* Accessed: June 2024, [online.] Available: https://functions.wolfram.com.
[50] R. J. Hill and R. G. Frehlich, "Probability distribution of irradiance for the onset of strong scintillation," *J. Opt. Soc. Am. A Optica Publishing Group*, vol. 14, no. 7, pp. 1530–1540, Jul 1997.
[51] H. Safi, A. Dargahi, J. Cheng, and M. Safari, "Analytical channel Model and Link Design Optimization for Ground-to-HAP Free-Space Optical Communications," *IEEE J. Light. Technol.*, vol. 38, no. 18, pp. 5036–5047, Sep 2020.